Adaptive beam combining and interferometry with photorefractive quantum wells

D. D. Nolte, T. Cubel,* and L. J. Pyrak-Nolte

Department of Physics, Purdue University, West Lafayette, Indiana 47907-1396

M. R. Melloch

School of Electrical and Computer Engineering, Purdue University, West Lafayette, Indiana 47907

We present a comprehensive study of excitonic electroabsorption and two-wave mixing in photorefractive quantum wells. By combining these two measurements, we are able to determine the internal grating writing efficiency for converting an external spatial light modulation into an internal space-charge field. The internal writing efficiency at a fringe spacing $\Lambda = 40\ \mu$m is found to be a decreasing function of applied field, varying from $\xi = 0.4$ at low fields to 0.2 at 12 kV/cm. The two-wave mixing efficiency in the quantum wells exceeds 40% and is used for adaptive beam combining and laser-based ultrasound detection. The quantum wells balance the hot-electron-induced photorefractive phase shift with excitonic spectral phase to guarantee quadrature in homodyne detection of ultrasound-induced surface displacements. The ability to tune through multiple quadratures is demonstrated here for the first time to our knowledge. We derive a noise-equivalent surface displacement of 1.7×10^{-6} Å (W/Hz)$^{1/2}$ at a field of 12 kV/cm and a fringe spacing of $\Lambda = 40\ \mu$m. This value is within a factor of 7 of the shot-noise limit of an ideal interferometer. © 2001 Optical Society of America

OCIS codes: 090.2880, 280.3420, 010.1080, 190.5330, 190.5970.

1. INTRODUCTION

Adaptive interferometers can compensate vibrations, speckle, or turbulence and have significant advantages over conventional nonadaptive interferometers. There has been sustained interest in finding appropriate materials to perform adaptive beam cleanup or adaptive beam combining that would provide the adaptive component in an interferometric system. Two-wave mixing in photorefractive crystals was demonstrated as a means to perform adaptive beam combining,[1] with initial application toward laser-based ultrasound detection.[2–4] Recent advances in the development of photorefractive CdTe[5] and InP[6] have led to performance near the ideal interferometric shot-noise limit. Photorefractive semiconductors have the advantage of large compensation bandwidths because of their fast grating refresh rates.

Photorefractive quantum wells[7] have the highest sensitivity of any photorefractive materials, with a sensitivity of $S_2 = 3 \times 10^6$ cm^2/J. These devices also have compensation bandwidths that approach 1 MHz.[8] This combination of sensitivity with speed makes them ideal candidates for adaptive beam combiners in laser-based ultrasound detection and other adaptive interferometric applications. The quantum wells are also compatible with inexpensive laser diodes. In an earlier study we demonstrated that adaptive homodyne mixing in photorefractive quantum wells approached the ideal interferometric shot-noise limit.[9] The quantum wells were shown to have a unique attribute, which we call excitonic spectral phase, not shared with any of the previous two-wave mixing demonstrations, that guarantees homodyne detec-tion in quadrature by simply adjusting the operating wavelength.

In this paper we present a comprehensive study of two-wave mixing and adaptive beam combining in photorefractive quantum wells. We begin by making an explicit connection between measured electroabsorption and measured two-wave mixing. The two-wave mixing performance in the quantum wells is complicated by several aspects of the device operation that have not previously been explored in detail. These aspects include the deviation from quadratic dependence of the electroabsorption at high electric fields, the onset of hot-electron effects associated with the Gunn effect in GaAs,[10] and the role of the excitonic spectral phase in achieving quadrature. We provide a complete experimental exploration of these effects and apply the results to predict the noise-equivalent surface displacement (NESD) for laser-based ultrasound detection using photorefractive quantum-well devices.

2. QUADRATIC ELECTRO-OPTICS

Electroabsorption based on quantum-confined excitons in a transverse field (field applied in the plane of the quantum wells) depends on only even powers of the applied electric field because of even symmetry with respect to the sign of the field. At low fields the change in absorption depends quadratically on the applied field, and at high fields the change in absorption shows pronounced deviation from pure quadratic dependence. The cross over from the low-field to high-field regimes depends on the strength of the quantum confinement.

A. Field-Dependent Absorption

The field-dependent changes in the optical function of a semiconductor are expressed in terms of the complex refractive index $\tilde{n}$, but the quantity that is most accessible to experimental measurement is absorption. The energy- and field-dependent absorption is expressed as

$$\alpha(h\nu, F) = \alpha^{(0)}(h\nu) + \frac{1}{2}\alpha^{(2)}(h\nu)F^2[1 + \rho(h\nu, F)],\tag{1}$$

where $\alpha^{(0)}$ is the zero-field absorption, $\alpha^{(2)}$ is the quadratic coefficient, F is the applied electric field, $h\nu$ is the photon energy, and $\rho(h\nu, F)$ is an even function that describes the deviation of the absorption from a quadratic dependence on field. The deviation is negative, causing the change in absorption to be smaller at higher fields than predicted by the quadratic coefficient.

The electroabsorption spectrum $\Delta\alpha(h\nu, F_0)$ of a semiconductor is given by the change in absorption in response to a static applied field F_0:

$$\Delta\alpha(h\nu, F_0) = \alpha(h\nu, F_0) - \alpha(h\nu, 0)$$

$$= \frac{1}{2}\alpha^{(2)}(h\nu)F_0^2[1 + \rho(h\nu, F_0)].\tag{2}$$

Experimentally, the electroabsorption can be obtained through differential transmission experiments performed with static fields by taking difference spectra. The electroabsorption is obtained as

$$\Delta\alpha(h\nu, F_0) = -\frac{1}{L}\ln\left[1 + \frac{T(h\nu, F_0) - T(h\nu, 0)}{T(h\nu, 0)}\right],\tag{3}$$

where the sample thickness is L. Equation (3) neglects Fabry–Perot effects that occur from Fresnel reflection from the sample surfaces. If the electroabsorption experiments are performed with ac fields, then Eqs. (2) and (3) must be modified to extract the electroabsorption from the Fourier coefficient measured in the experiment.

B. Experimental Electroabsorption and Electrorefraction

Differential transmission data were obtained on growth structure 101196D grown by molecular beam epitaxy at 600 °C on a semi-insulating substrate. The active electro-optic layers consisted of 100 periods of 70-Å GaAs and 60-Å $Al_{0.3}Ga_{0.7}As$. The superlattice was proton implanted after growth with two doses of $1 \times 10^{12}\,cm^{-2}$ at energies of 80 and 160 keV to make it semi-insulating. The quantum wells were grown on a stop-etch layer of 5000 Å of $Al_{0.5}Ga_{0.5}As$, which permitted the samples to be epoxied to glass and the substrate removed to perform optical transmission experiments. Titanium–gold contacts were evaporated on the top surface before epoxying. The contacts are used to apply transverse electric fields to operate the quantum wells in the transverse Franz–Keldysh geometry.[7,11,12]

The differential transmission spectra on device IL338[9] from growth 101196D are shown in Fig. 1 for electric fields from 5 kV/cm to 25 kV/cm. The change in absorption $\Delta\alpha$ owing to the applied electric fields is shown in Fig.

2. We observed a large electroabsorption approaching 6000 cm^{-1}, which, to our knowledge, is the largest absorption change observed to date in transverse-field photorefractive quantum wells.

The departure from quadratic dependence on the applied electric field is described by the function $\rho(h\nu, F)$ discussed above. This was measured at a wavelength near the heavy-hole exciton resonance. Figure 3 shows the dependence of the differential transmission as a function of the applied electric field at the heavy-hole exciton energy.[13] The deviation from quadratic behavior results in a smaller differential transmission (and hence a smaller electroabsorption) than predicted by the quadratic coefficient. The solid curve in Fig. 3 shows the quadratic behavior, and the deviation from this behavior is shown as the dashed line. The dashed line can be described as a quadratic function,

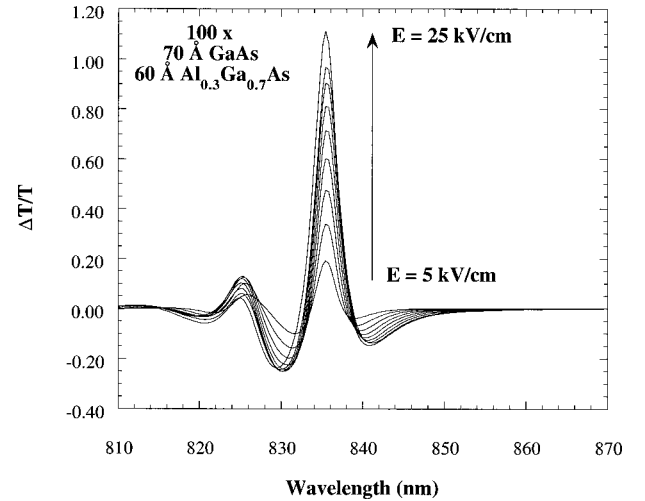$$\rho(h\nu, F) \approx -\frac{1}{2}\rho_1 F^2,\tag{4}$$

Fig. 1. Differential transmission $\Delta T/T$ data as a function of wavelength for increasing dc electric fields. Reprinted from Ref. 9.
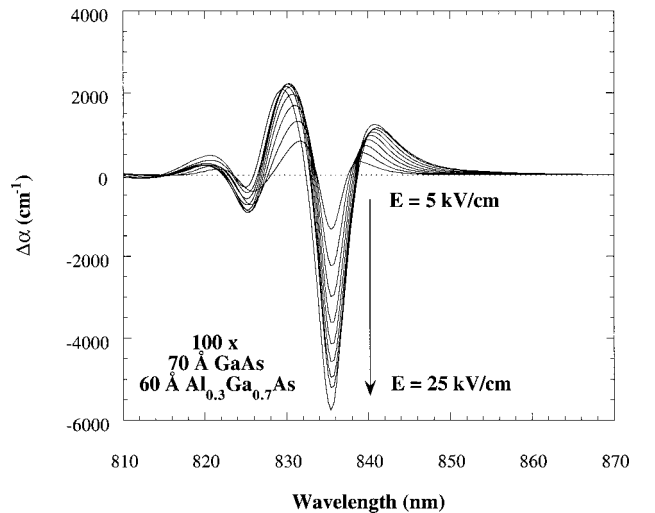

Fig. 2. Electroabsorption $\Delta\alpha$ as a function of wavelength extracted from the data in Fig. 1.
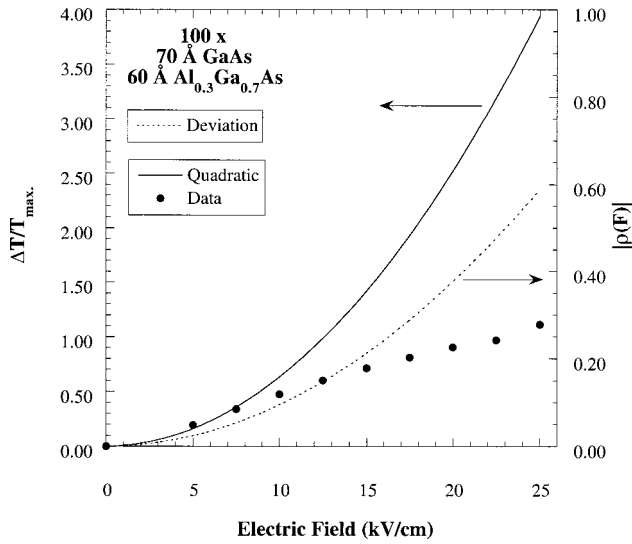
Fig. 3. Plot of the maximum differential transmission shown with the low-field quadratic fit. The deviation from quadratic behavior is shown as the dashed curve.
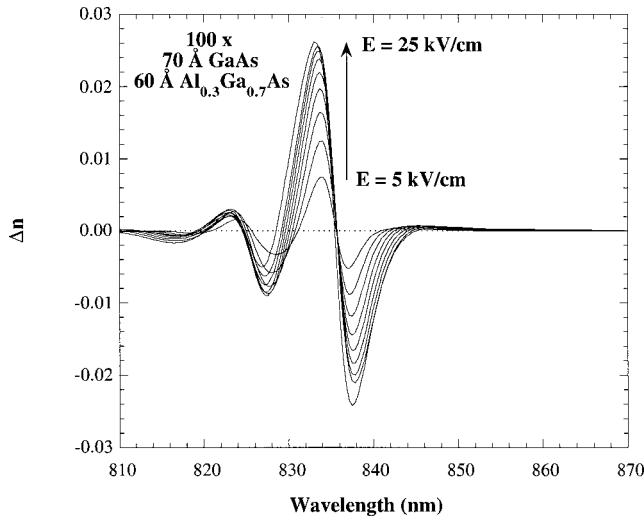

Fig. 4. Electrorefraction Δn obtained through a Kramers–Kronig transform of the electroabsorption in Fig. 2.

where ρ_1 is the positive coefficient. The departure from quadratic behavior is small at low electric fields (<7 kV/cm in these devices). At high applied electric fields the deviation from quadratic behavior can be large, reducing the electroabsorption and electrorefraction in the device. A value of $\rho_1 = 2 \times 10^{-3}$ cm^2/kV^2 is obtained from the data in Fig. 3. This can produce significant effects in the photorefractive process that transforms the spatially modulated electric field into the absorption and index gratings that are the source of two-wave mixing in the photorefractive quantum wells.

The changes in the absorption spectrum are accompanied by changes in the refractive index in the material through the Kramers–Kronig transformation:

$$\Delta n(\lambda) = -\frac{\lambda^2}{2\pi^2} P \int_0^\infty \frac{\Delta \alpha(\lambda)}{\lambda'^2 - \lambda^2} d\lambda'. \qquad (5)$$

The calculated change in the refractive index Δn is shown in Fig. 4. The fractional change in index ($\Delta n/n$) approaches 1%. These large changes in the absorption and index are necessary ingredients for good signal-to-noise detection in an adaptive homodyne interferometer.

3. TWO-WAVE MIXING

A. Associating Photorefractive Gratings with Electroabsorption

Photorefractive two-wave mixing in semiconductor quantum wells and thin films provides a versatile spectroscopy of both the electro-optic properties of the materials as well as the electronic transport and space-charge properties of the transverse-field devices. In two-wave mixing between a signal beam (I_1) and a pump beam (I_2) the two beams produce an intensity pattern in the sample given by

$$I(x) = (I_1 + I_2)[1 + m \cos(Kx)], \qquad (6)$$

where K is the grating vector, given by $K = 2\pi/\Lambda$, where Λ is the interference fringe spacing. When the beams are incident symmetrically relative to the normal of the quantum-well surface, the grating lies in the plane of the thin film. The modulation index m is

$$m = \frac{2\sqrt{I_1 I_2}}{I_1 + I_2} = \frac{2\sqrt{\beta}}{1 + \beta}, \qquad (7)$$

where the beam ratio $\beta = I_2(0)/I_1(0)$.

In the photorefractive process[14] the intensity pattern is imprinted into the photorefractive material as a spatial modulation of internal space charge. Under an applied electric field F_0, the internal space charge (to first order) is expressed by

$$F(x) = F_0[1 - m\xi \cos(Kx + \phi_P)], \qquad (8)$$

where ϕ_P is the photorefractive phase shift. Photorefractive phase shifts are common in many photorefractive materials and have different physical origins. Photorefractive phase shifts were discovered in transverse-field photorefractive quantum wells[15] and have been shown to arise from hot-electron effects and transport nonlinearity.[10,16] In Eq. (8) the modulation amplitude is given by the index m multiplied by a parameter ξ, which expresses the contrast ratio of the field within the device relative to the modulation expressed by Eq. (7). Most of the electron-transport physics of the photorefractive effect is contained within the two parameters ϕ_P and ξ. These dynamics will not be considered in the development here because some of these effects have been addressed in previous references.[8,11,16] However, the writing efficiency ξ has not previously been measured to our knowledge.

In the following derivations we assume a harmonic response of the internal space-charge field to the intensity pattern. This assumption is valid under many operating conditions and will lead to results that are relevant for usual circumstances. The sinusoidal space-charge field produces a corrugated absorption grating given by

$$\alpha(h\nu, x) = \alpha_0(h\nu) + \alpha_K(h\nu)\cos(Kx + \phi_P). \qquad (9)$$

One of the goals of this paper is to compare the experimentally measured electroabsorption $\Delta\alpha$ with the two-wave mixing response. Therefore we can express the absorption grating in terms of the electroabsorption measured for the same field F_0 by

$$\alpha_0(h\nu) = \alpha^{(0)}(h\nu) + \frac{\Delta\alpha(h\nu, F_0)}{1 + \rho(h\nu, F_0)}\left(1 + \frac{1}{2}m^2\xi^2\right)$$
$$+ \frac{\Delta\alpha(h\nu, F_0)}{F_0^2\Lambda}\int_0^\Lambda F(x)^2\rho[h\nu, F(x)]\mathrm{d}x, \quad (10)$$

$$\alpha_K(h\nu) = -\frac{\Delta\alpha(h\nu, F_0)}{1 + \rho(h\nu, F_0)}2m\xi$$
$$+ \frac{2\Delta\alpha(h\nu, F_0)}{F_0^2\Lambda}\int_0^\Lambda F(x)^2\rho[h\nu, F(x)]\cos(Kx$$
$$+ \phi_P)\mathrm{d}x, \quad (11)$$

where the deviation from quadratic field dependence is given by $\rho(h\nu, F_0)$.

When the approximation for $\rho(h\nu, F)$ from Eq. (4) is used, Eqs. (10) and (11) can be evaluated explicitly to be

$$\alpha_0(h\nu) = \alpha^{(0)}(h\nu) + \Delta\alpha(h\nu, F_0)\left(1 + \frac{1}{2}m^2\xi^2\right)$$
$$- \Delta\alpha(h\nu, F_0)\frac{1}{2}\rho_1 F_0^2\left(\frac{5}{2}m^2\xi^2 + \frac{3}{8}m^4\xi^4\right),$$
$$(12)$$

$$\alpha_K(h\nu) = \Delta\alpha(h\nu, F_0)\left[-2m\xi + \frac{1}{2}\rho_1 F_0^2(2m\xi + 3m^3\xi^3)\right].$$
$$(13)$$

The associated Fourier coefficient for the refractive index is

$$n_K(h\nu) = \Delta n(h\nu, F_0)\left[-2m\xi + \frac{1}{2}\rho_1 F_0^2(2m\xi + 3m^3\xi^3)\right],$$
$$(14)$$

where $\Delta n(h\nu, F_0)$ is derived from $\Delta\alpha(h\nu, F_0)$ by use of the Kramers–Kronig relation. These expressions [Eqs. (12)–(14)] are valid to all orders of m and ξ and to first order in ρ_1. Note that the deviation from quadratic electroabsorption acts to reduce the Fourier coefficients of the photorefractive gratings [ρ_1 is a positive quantity, defined in Eq. (4)].

In the low-field limit these expressions simplify to

$$\alpha_0(h\nu, F_0) = \alpha^{(0)}(h\nu) + \Delta\alpha(h\nu, F_0)\left(1 + \frac{1}{2}m^2\xi^2\right),$$

$$\alpha_K(h\nu, F_0) = -\Delta\alpha(h\nu, F_0)2m\xi,$$

$$n_K(h\nu, F_0) = -\Delta n(h\nu, F_0)2m\xi. \quad (15)$$

It is important to keep in mind that the Fourier coefficients of the photorefractive gratings in Eq. (15) must be related to the electroabsorption $\Delta\alpha$ and electrorefraction Δn measured under identical applied field strength F_0. In addition, the zero-order Fourier coefficient in Eq. (15) contains a contribution from the modulated field. The

average transmission during two-wave mixing is therefore a function of both the applied electric field and the modulation depth of the interference between the two mixing beams.

We can define an effective ξ_{eff} that can be measured experimentally through combined two-wave mixing experiments and electroabsorption experiments as

$$\xi_{\text{eff}} = \frac{\alpha_K(h\nu)}{2m\Delta\alpha(h\nu)} = \xi\left[1 - \frac{1}{2}\rho_1 F_0^2\left(1 + \frac{3}{2}m^2\xi^2\right)\right].$$
$$(16)$$

The expression in brackets is a decreasing function of applied field, even in the case of small modulation. This decrease in ξ_{eff} will partially cancel the advantages for two-wave mixing of increased electroabsorption at high fields.

B. Two-Wave Mixing

In two-wave mixing the two writing beams I_1 and I_2 self-diffract, with the first diffraction order of each copropagating with the transmitted order of the other beam. The diffracted amplitudes are calculated in the Raman–Nath regime by assuming that the hologram in the thin film modifies the transmitted intensity as

$$E_1(x, L) = E_1(x, 0)\exp\{i[\delta_0 + \delta_1\cos(Kx + \phi_P)]\},$$
$$(17)$$

where the complex phase with Fourier index K is given by

$$\delta_K = \frac{2\pi n_K(h\nu, F_0)L}{\lambda\cos\theta'} + i\frac{\alpha_K(h\nu, F_0)L}{2\cos\theta'}, \quad (18)$$

where n_K and α_K are obtained from Eqs. (13) and (14).

The amplitude of the signal beam after passing through the dielectric film and mixing with the diffracted amplitude of the pump beam is

$$E_1(E_2, L) = J_0(\delta_1)E_1(0)\exp(i\delta_0)$$
$$+ J_1(\delta_1)E_2(0)\exp[i(\delta_0 + \phi_P + \pi/2)],$$
$$(19)$$

where the Bessel functions describe the Raman–Nath diffraction.[17] The diffracted component of the pump beam acquires a phase equal to the photorefractive phase shift ϕ_P and also is shifted by $\pi/2$ relative to the signal beam. It is important to note that δ_1 is complex, and an additional phase is acquired by the diffracted pump relative to the signal beam. This additional phase is called the excitonic spectral phase and is described in Section 5.

The corresponding intensity for $I_1(L)$ is given by

$$I_1(I_2, L) = \eta_0 I_1(0)\exp(-\alpha_0 L)$$
$$+ \eta_1 I_2(0)\exp(-\alpha_0 L)$$
$$+ 2\sqrt{I_1(0)I_2(0)}\exp(-\alpha_0 L)$$
$$\times \{\text{Re}[J_1(\delta_1)J_0(\delta_1^*)]\sin\phi_P$$
$$- \text{Im}[J_1(\delta_1^*)J_0(\delta_1)]\cos\phi_P\}, \quad (20)$$

and a similar expression for intensity $I_2(L)$ is

$$I_2(I_1, L) = \eta_0 I_2(0)\exp(-\alpha_0 L) + \eta_1 I_1(0)\exp(-\alpha_0 L)$$
$$+ 2\sqrt{I_1(0)I_2(0)}\, \exp(-\alpha_0 L)$$
$$\times \{\mathrm{Re}[J_{-1}(\delta_1)J_0(\delta_1^*)]\sin\phi_P$$
$$+ \mathrm{Im}[J_{-1}(\delta_1^*)J_0(\delta_1)]\cos\phi_P\}, \tag{21}$$

where the diffraction efficiencies of order M are

$$\eta_M = J_M(\delta_1)J_M(\delta_1^*). \tag{22}$$

These diffraction efficiencies are defined as output diffraction efficiencies that are given by the ratio of the diffracted intensity to the transmitted intensity.

By expanding the Bessel functions to lowest order, the intensities of the two emerging beams at $z = L$ relative to the intensities of the incident beams at $z = 0$ can be expressed as[11]

$$I_1(I_2, L) = \exp[-\alpha_0(F_0)L]$$
$$\times \left\{ I_1(0) - \sqrt{I_1(0)I_2(0)}\left[\frac{\alpha_K(h\nu, F_0)L}{2\cos\theta'}\cos\phi_P \right.\right.$$
$$+ \left.\left. \frac{2\pi n_K(h\nu, F_0)L}{\lambda\cos\theta'}\sin\phi_P \right]\right\}$$

$$I_2(I_1, L) = \exp[-\alpha_0(F_0)L]$$
$$\times \left\{ I_2(0) - \sqrt{I_1(0)I_2(0)}\left[\frac{\alpha_K(h\nu, F_0)L}{2\cos\theta'}\cos\phi_P \right.\right.$$
$$- \left.\left. \frac{2\pi n_K(h\nu, F_0)L}{\lambda\cos\theta'}\sin\phi_P \right]\right\}. \tag{23}$$

The contribution to the transmitted intensity from the absorption grating is symmetric with respect to the photorefractive phase shift ϕ_P, whereas the contribution from the index grating is asymmetric. By reversing the direction of the applied electric field, it is possible to determine both contributions.

The two-wave mixing efficiency is defined in terms of the difference in the transmitted signal intensity in the presence of mixing minus the signal intensity in the absence of mixing (no pump beam, but still under applied field F_0), divided by the zero-mixing transmission:

$$\frac{\Delta I}{I} = \frac{I_1(I_2, F_0, L) - I_1(0, F_0, L)}{I_1(0, F_0, L)}. \tag{24}$$

By use of the small-signal expressions in Eqs. (15) and (23) this becomes

$$\frac{\Delta I}{I} = \exp\left[-\Delta\alpha(F_0)L\frac{1}{2}m^2\xi^2 \right]$$
$$\times \left\{ -\frac{1}{2}m^2\xi^2\Delta\alpha(F_0)L + \frac{2\beta}{1+\beta}\xi\left[\frac{\Delta\alpha(F_0)L}{\cos\theta'}\cos\phi_P \right.\right.$$
$$+ \left.\left. \frac{4\pi\Delta n(F_0)L}{\lambda\cos\theta'}\sin\phi_P \right]\right\}. \tag{25}$$

This equation directly relates the measured electroab-

sorption $\Delta\alpha$ (and electrorefraction Δn through Kramers–Kronig) to the measured two-wave mixing efficiency $\Delta I/I$. The equation includes the modulation index m, which is defined by the beam ratio β, which can be measured. Therefore Eq. (25) can be used to extract ξ and ϕ_P from a pair of electroabsorption and two-wave mixing experiments performed at a given field.

C. Experimental Studies of Two-Wave Mixing

Two multiple-quantum-well structures were used in the two-wave mixing study. The growths 020197B and 101196D each contained 100 periods of 7-nm GaAs wells and 6-nm $Al_{0.3}Ga_{0.7}As$ barriers. The multiple-quantum-well regions were sandwiched between buffer epilayers of $Al_{0.2}Ga_{0.8}As$. Growth 020197C had a *p*-doped contact layer that was 40 nm thick with a doping density of $1 \times 10^{19}\,\mathrm{cm}^{-3}$ grown after the stop-etch layers, whereas growth 101196D had no extra contacting layer. Both devices were fabricated by removing the substrates for transmission studies. Coplanar electrical contacts of Ti–Au were used for both growths with a gap of 1 mm. These were applied to the doped layer for growth 020197C after a window was etched into the AlGaAs epilayer buffer to prevent shorting of the device. For devices fabricated from 101196D the contacts were either applied on the free surface after removing the substrate or were applied on the top surface before removing the substrate. The top contacts were buried in epoxy, which acts to passivate the surface of the devices. These buried contact devices could sustain electric fields up to 25 kV/cm. The free-surface contact devices could support fields only up to 17 kV/cm before surface breakdown would occur. The devices were proton implanted at total doses of $2 \times 10^{12}\,\mathrm{cm}^{-2}$ or $3 \times 10^{11}\,\mathrm{cm}^{-2}$ with two energies of 80 keV and 160 keV. The proton implantation renders the undoped material semi-insulating.

The two-wave mixing data for device JAC44 from growth 020197C are shown in Fig. 5 as a function of electric field and grating spacing for a fixed wavelength of 838 nm and $\beta = 1$. The grating period was varied between 4.4 mm and 97 mm, and the field was varied between -10 kV/cm and $+10$ kV/cm. It has been well documented
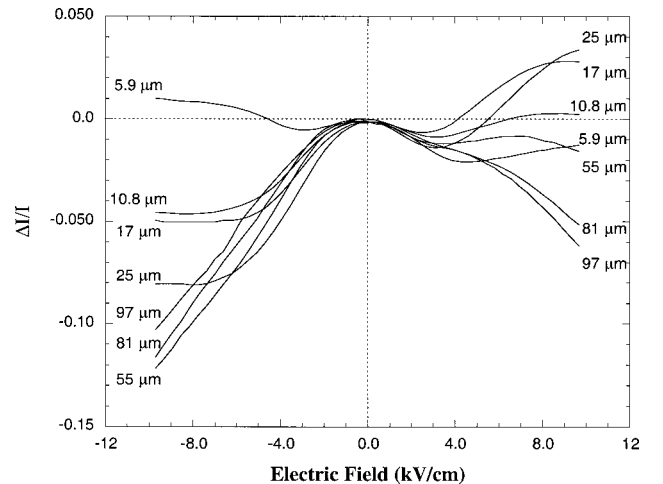
Fig. 5. Two-wave mixing at a fixed wavelength as a function of electric field for a family of different fringe spacings.

that the phase shift in Eq. (23) is field dependent.[10] This field dependence of the phase shift makes the fixed-wavelength field-dependent data extremely complex. The data are asymmetric in the electric field, reflecting the asymmetry of the Δn term in Eq. (25) as the phase changes sign with the electric field sign. Phase shifts are small at small field,[10] which is reflected in the approximately symmetric quadratic low-field behavior.

Because of the complicated interdependences of the phase shift on fringe spacing, wavelength, and electric field, it is not possible to extract either ξ or ϕ_P from the single-wavelength data of Fig. 5. We therefore obtained fixed-field two-wave mixing spectra by tuning the laser with computer control and acquisition. Two-wave mixing experiments were performed with an EOSI 2000 tunable diode laser with a maximum power of 20 mW, tunable from 825 nm to 845 nm. The experiment was computer controlled to scan the laser and acquire data from a lock-in amplifier or an oscilloscope. The beam ratio β was set to 1 and 16. Spectra in a series are shown in Figs. 6 and 7 as a function of wavelength for increasing electric field on device IL341 for growth 101196D for our two values of β with a fringe spacing of 40 μm. Individual spectra at ±1200 kV/cm are shown in Fig. 8 for β = 16. The asymmetry in the sign of the applied field is evident in the shifts in the zero crossings (where the signal changes sign) in the data.
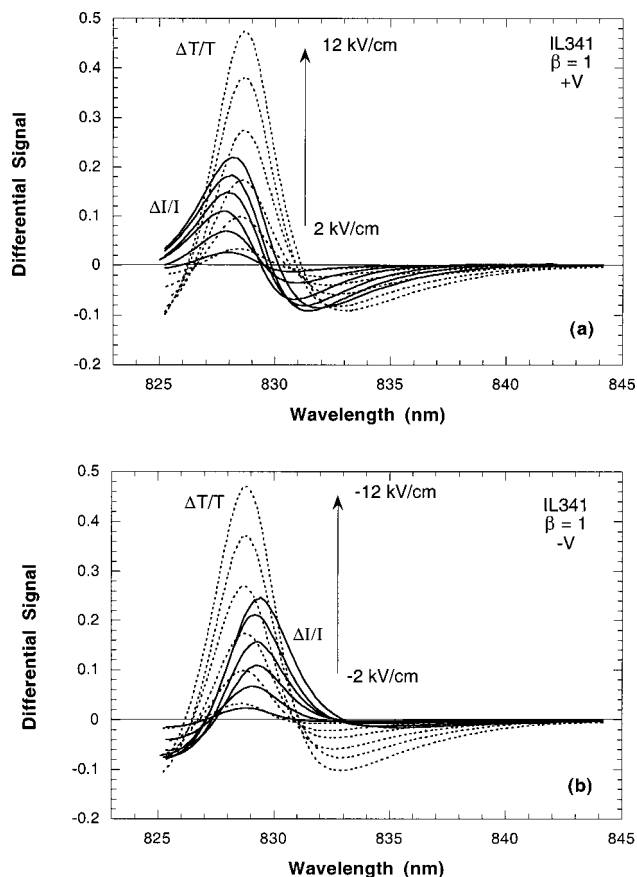

Fig. 6. Differential transmission $\Delta T/T$ and two-wave mixing signal $\Delta I/I$ spectra for $\beta = 1$ and $\Lambda = 40\,\mu$m with increasing field strength, showing results for both positive and negative fields.
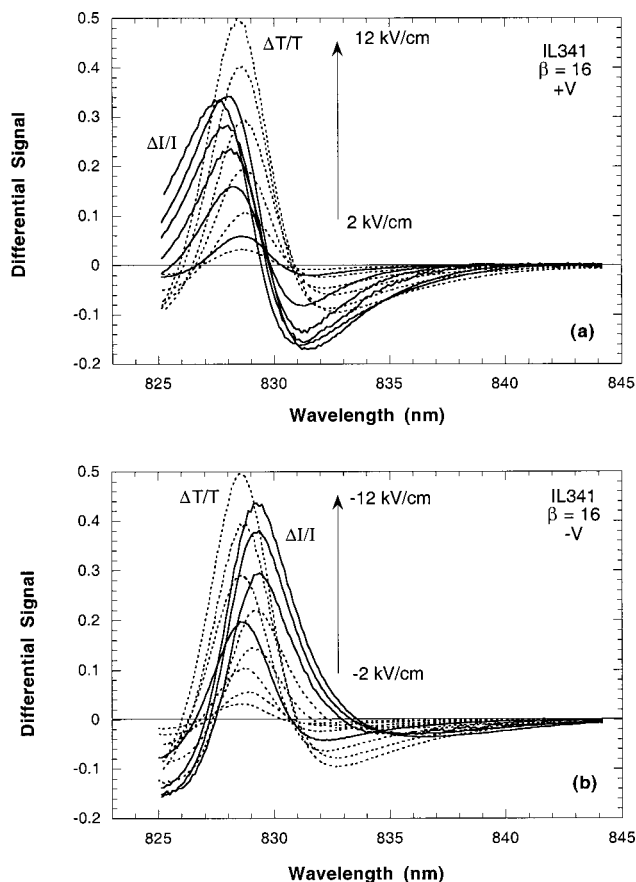

Fig. 7. Differential transmission $\Delta T/T$ and two-wave mixing signal $\Delta I/I$ spectra for $\beta = 16$ and $\Lambda = 40\,\mu$m with increasing field strength, showing results for both positive and negative fields. The two-wave mixing efficiency is greater than 40% for a field of -12 kV/cm.
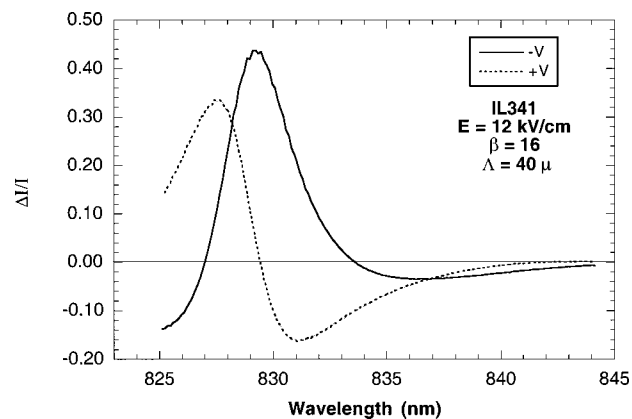

Fig. 8. Two-wave mixing spectrum for positive and negative fields at 12 kV/cm, showing the asymmetry caused by the photorefractive phase shift.

By simultaneously measuring electroabsorption and two-wave mixing, it is possible to use Eq. (25) to fit values for ξ and ϕ_P. The field-dependent values of ξ or ϕ_P are shown in Fig. 9 for a fringe spacing of 40 μm. The value of ξ varies between 40% at low field and 20% at high field. The phase shift is asymmetric in the applied field and approaches $\pm0.7\pi/2$ at fields of ±12 kV/cm, which is consistent with earlier measurements.[10]

4. PHASE MODULATION AND ADAPTIVE HOMODYNE DETECTION

Self-diffraction from the hologram in the photorefractive quantum well acts as a means to combine the signal beam with the reference beam. The hologram adapts to slowly varying phases but cannot adapt to rapidly varying phases (at frequencies above the adaptive bandwidth of the photorefractive quantum well). Two-wave mixing therefore performs adaptive beam combining for adaptive interferometry applications in which low frequencies are compensated, but high frequencies are passed downstream on a signal beam that copropagates with the reference beam. One application is the homodyne detection of ultrasound. An oscillating surface that has a displacement given by $d(t)$ produces a phase modulation in a reflected beam of

$$\phi(t) = -\frac{4\pi}{\lambda} d(t). \tag{26}$$

The combined signal and reference fields are then given by

$$E_1(E_2, L) = J_0(\delta_1)E_1(0)\exp(i\,\delta_0) + J_1(\delta_1)E_2(0)$$
$$\times \exp\left\{ i\left[\delta_0 + \phi_P - \frac{4\pi}{\lambda} d(t) + \pi/2 \right] \right\}, \tag{27}$$
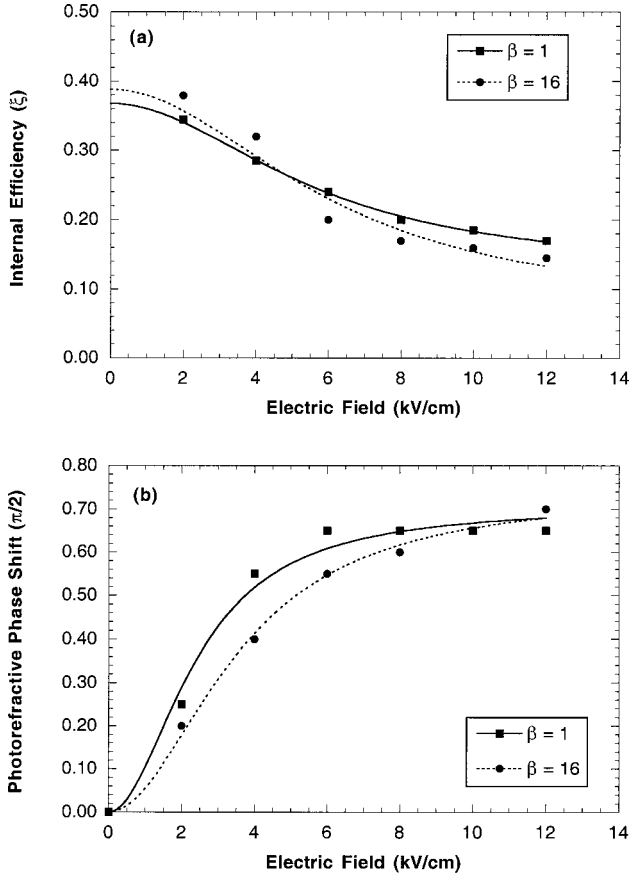

Fig. 9.   Plot of (a) the internal writing efficiency ξ versus field strength for $\beta = 1$ and 16 and (b) the photorefractive phase shift. These graphs are obtained by fitting the data of Figs. 6 and 7 to the theoretical differential intensity derived from Eq. (25).

where δ_i is given in Eq. (18).   Expanding the Bessel functions, this becomes

$$E_1(E_2, L) = E_1(0)\exp(i\,\delta_0) + \frac{1}{2}\delta_1 E_2(0)$$
$$\times \exp\left\{ i\left[\delta_0 + \delta_P - \frac{4\pi}{\lambda} d(t) + \pi/2 \right] \right\}. \tag{28}$$

It is important to remember that δ_1 in the last expression is an analytic function of λ. It can therefore be expressed as a wavelength-dependent amplitude and a phase,

$$\delta_1 = |\delta_1|\exp(i\,\psi), \tag{29}$$

where

$$\frac{1}{2}|\delta_1| = \sqrt{\eta(\lambda)} = \sqrt{\left[\frac{\pi n_1(\lambda)L}{\lambda\cos\theta'}\right]^2 + \left[\frac{\alpha_1(\lambda)L}{4\cos\theta}\right]^2}, \tag{30}$$

and the phase

$$\psi(\lambda) = \tan^{-1}\left[\frac{\lambda}{4\pi}\frac{\alpha_1(\lambda)}{n_1(\lambda)}\right], \tag{31}$$

which we call the excitonic spectral phase. With this definition, Eq. (28) becomes

$$E_1(E_2, L) = \exp(i\,\delta_0)\Bigg(E_1(0) + \sqrt{\eta(\lambda)}E_2(0)$$
$$\times \exp\left\{ i\left[\phi_P + \psi(\lambda) - \frac{4\pi}{\lambda} d(t) + \pi/2 \right] \right\}\Bigg). \tag{32}$$

The optimal homodyne detection occurs when the time-independent relative phase of the signal beam relative to the diffracted reference beam is equal to $\pi/2$. From Eq. (32) this condition is satisfied when

$$\phi_P = -\psi(\lambda). \tag{33}$$

This condition satisfies the requirements for linear detection of the surface displacement $d(t)$.

The photorefractive phase shift ϕ_P of the photorefractive quantum wells is a function of the applied electric field, the fringe spacing, and the defect density. The unique feature of the photorefractive quantum wells is that the condition in Eq. (33) can always be satisfied for any photorefractive phase shift ϕ_P by tuning the wavelength λ through the wavelength range of the excitonic absorption.

5. EXCITONIC SPECTRAL PHASE

The feature that makes photorefractive quantum wells unique for adaptive homodyne detection is the excitonic spectral phase $\psi(\lambda)$. The remarkable aspect of this phase is that it appears on equal terms with the photorefractive phase shift in Eq. (33), and yet it has an entirely different origin. The photorefractive phase shift represents a physical shift of the hologram relative to the opti-

cal fringe pattern. It contributes to the relative optical phase of the combined beams because it adjusts the optical path length of the diffracted beam relative to the transmitted beam. Although the photorefractive phase shift has its origins in the dynamics of photorefractive grating formation, it contributes to the optical phase in a purely kinematic sense; it alters optical path lengths but is unrelated to the physical (dynamical) processes that give rise to the refractive index in the material. The excitonic spectral phase also contributes to the relative optical phase between the signal and reference beams, but it has a purely dynamical origin in the dielectric response of the material to electromagnetic fields. Therefore the condition in Eq. (33) for optimum linear detection of homodyne signals equates a kinematic phase with a dynamical phase. This situation is unique to the photorefractive quantum wells.

The dynamical origin of the excitonic spectral phase rests in the excitonic resonances. The exciton is a quantum-mechanical oscillator that is driven by incident electromagnetic fields. As in any mechanical oscillation, the frequency of excitation can be tuned through the resonance. The linear response to the drive frequency has a resonant line shape with an associated phase that changes as the frequency varies from below resonance to above resonance. In the case of excitonic absorption the linear response leads to a resonance-enhanced refractive index (dispersion), whereas damping leads to absorption. The shift in the phase is obtained by taking the inverse tangent of the ratio between the absorption and the dispersion, as given in Eq. (31).

The wavelength-dependent excitonic spectral phase $\psi(\lambda)$ is shown in Fig. 10 for the multiple field conditions from Fig. 1. The phase varies nearly linearly with wavelength through the excitonic resonances of the heavy and the light holes and is relatively insensitive to the value of the electric field. The phase change through the entire spectrum is approximately equal to 6π. Each lobe of either the electroabsorption spectrum (Fig. 2) or the electrorefraction spectrum (Fig. 4) contributes one π. The spectra each contain approximately six lobes (within the wavelength range of the spectra), adding to a total phase
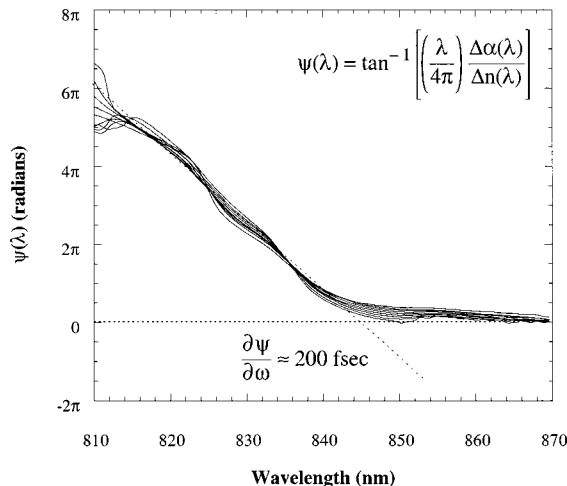
change of 6π. It is important to note that additional contributions to the phase should occur at higher energies owing to Franz–Keldysh oscillations. However, these are below our detection sensitivity in these experiments.

The linear dependence of the excitonic spectral phase on wavelength is important for the use of photorefractive quantum wells for femtosecond pulse-processing applications[18,19] in which the pulses remain transform limited. Designing photorefractive quantum-well devices to have linear excitonic spectral phase is a key aspect of the design of these devices for the femtosecond applications.[20] The excitonic spectral phase also contributes a group time delay to diffracted ultrafast pulses. The pulses are delayed by an amount equal to $\tau_{group} = d\psi/d\omega$, which is approximately 200 fs for the transverse-field photorefractive quantum wells. In the case of homodyne detection of laser-based ultrasound, the linearity of $\psi(\lambda)$ with wavelength is not essential, as long as the function is monotonic and can be tuned by adjusting the wavelength of the laser beams to achieve quadrature.

6. LASER-BASED DETECTION OF ULTRASOUND

A. Homodyne Detection

The change in signal I_1 caused by a surface displacement $d(t)$ is obtained from Eq. (32) as

$$\delta I_1 = 2\sqrt{I_1(0)I_2(0)} \exp(-\alpha L)\sqrt{\eta(\lambda)}$$
$$\times \cos\left[\phi_P + \psi(\lambda) + \frac{\pi}{2} + \frac{4\pi}{\lambda}d(t)\right], \quad (34)$$

which becomes, when $d(t)$ is small,

$$\delta I_1 = -2\sqrt{I_1(0)I_2(0)} \exp(-\alpha L)\sqrt{\eta(\lambda)}$$
$$\times \cos[\phi_P + \psi(\lambda)]\frac{4\pi}{\lambda}d(t), \quad (35)$$

taking only lowest order in the surface displacement $d(t)$.

Measured ultrasound signals are shown in Fig. 11 that are received from a gold-plated microscope cover slip that was excited with a conventional 2-MHz damped Panametrics piezoelectric transducer driven by a Panametrics model PR500 pulse generator. The arriving compressional (P) and shear (S) waves can be distinguished in the received waveforms, as well as later arriving energy that is probably due to reflections in the thin cover slip. The signals were amplified by 60 db with an amplifier bandwidth of 2 MHz and 100 averages on the digital oscilloscope. The physical surface displacements of the mirror are in a range around 100 pm. The device was operated at a field of 7.5 kV/cm with a fringe spacing of 30 μm. The traces show the mixing signal for several wavelengths between 836 nm and 831 nm, showing the tuning from a maximum in one quadrature to the maximum in an opposite quadrature. The exciton peak in this sample is near 836 nm. By tuning the wavelength of the laser, we demonstrate the role of the excitonic spectral phase, as

Fig. 10. Excitonic spectral phase $\Psi(\lambda)$ as a function of wavelength for the field-dependent data in Figs. 2 and 4.

well as the change in sign of the ultrasound signal as the wavelength is tuned out of one quadrant and into another.

Several new features are demonstrated in Fig. 11 that were not present in our earlier waveforms in Ref. 9. First, we demonstrate the change in sign of the ultrasound signal as we tune from one quadrant to another. Second, the data in Fig. 11 are raw data captured directly on the digital oscilloscope without subtracting background nonadaptive traces that arose in our earlier research from slight intensity changes in the signal beam. The ability to remove nonadaptive intensity changes is an important step forward toward applications. Third, the data in Fig. 11 were acquired with a fringe spacing of 30 μm, rather than the 200-μm fringe spacing of Ref. 9. This smaller fringe spacing is also an important step for applications because it allows for reasonable field-of-view for the ultrasound applications.

B. Noise-Equivalent Surface Displacement

The most important aspect of homodyne detection is the signal-to-noise ratio. If the detection is limited only by shot noise, the signal-to-noise ratio is given by

$$\frac{S}{N} = \frac{\delta P_1}{\sqrt{P_1(0)\exp(-\alpha_0 L)\dfrac{\Delta f \cdot h\nu}{-\zeta_{\mathrm{det}}}}}, \tag{36}$$

where $P_1(0)$ is the incident power on the photorefractive quantum well in the signal beam, Δf is the detection bandwidth, $h\nu$ is the photon energy, and ζ_{det} is the quantum efficiency of the detector. The signal-to-noise ratio becomes

$$\frac{S}{N} = 2\sqrt{\frac{P_2(0)\zeta_{\mathrm{det}}}{h\nu\Delta f}}\exp(-\alpha_0 L/2)\sqrt{\eta(\lambda)}$$

$$\times \cos[\phi_P + \psi(\lambda)]\frac{4\pi}{\lambda}\mathrm{d}(t). \tag{37}$$

Another parameter used to characterize a laser ultrasonic receiver is the minimum-detectable surface-displacement amplitude, called the noise-equivalent sur-
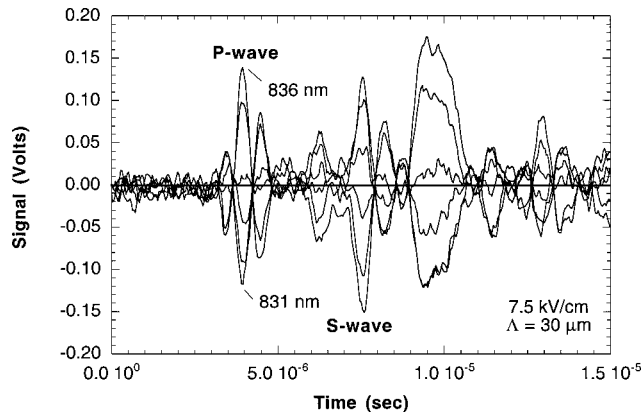
Fig. 11. Laser-based ultrasound time traces as the laser wavelength is tuned from one quadrature to the opposite quadrature. The arrival of the compressional (P) and shear (S) waves are clearly observed.
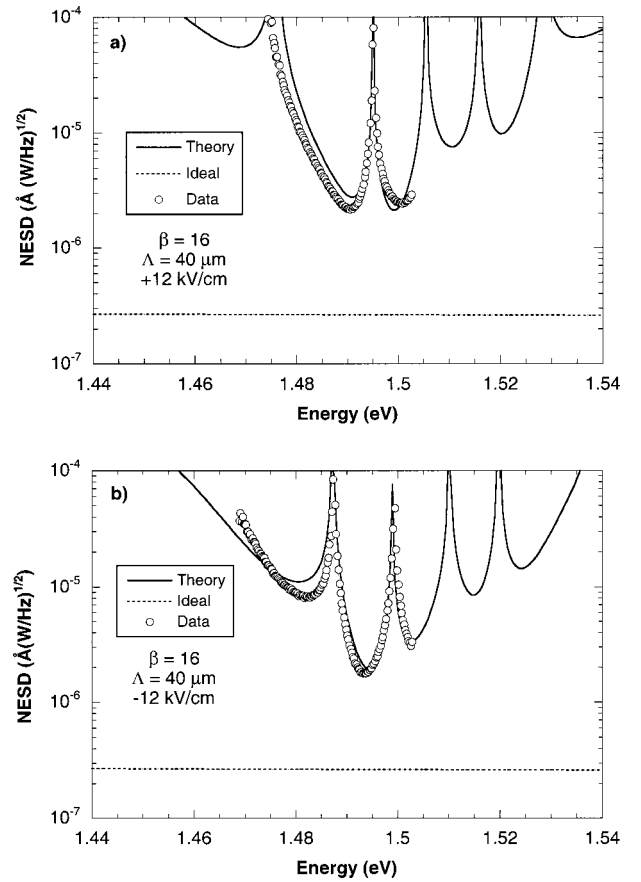
Fig. 12. Noise-equivalent surface-displacement NESD as a function of wavelength for (a) positive field and (b) negative field. The theoretical curve is from Eq. (38) with the parameters from Fig. 9. Also shown in the figure is the ideal shot-noise limit of a perfect interferometer.

face displacement (NESD). This parameter corresponds to the minimum-detectable displacement for which $S/N = 1$ for 1-W incident power and 1-Hz detection bandwidth. With this definition the NESD can be written as

$$d_{\min}(\lambda) = \frac{\lambda}{4\pi}\frac{1}{2\sqrt{\eta(\lambda)}\cos[\phi_P + \psi(\lambda)]}$$

$$\times \exp(\alpha_0 L/2)\sqrt{\frac{h\nu}{\zeta_{\mathrm{det}}}}, \tag{38}$$

where the minimum-detectable displacement is a function of wavelength and is a minimum near the center wavelength of the excitonic transitions because $\eta(\lambda)$ is maximum near the heavy-hole exciton transition. As the argument of the cosine changes, the NESD has poles corresponding to in-phase conditions and minima corresponding to quadrature conditions. The wavelengths where these conditions occur change when the photorefractive phase shift ϕ_P is altered by adjusting the electric field.

The NESD for photorefractive quantum-well sample IL341 is shown in Fig. 12 for both field directions. The data are compared against the theory from Eq. (38), with the values of ϕ_P and ξ from Fig. 9. The smallest value for the NESD is approximately $d_{\min} = 1.7$

$\times$ 10^{-6} Å$(W/Hz)^{1/2}$.   By comparison, the detection limit for an ideal interferometer is 2.6×10^{-7} Å$(W/Hz)^{1/2}$, which is approximately a factor of 7 smaller.   We have therefore achieved adaptive beam combining using experimental conditions that are compatible with laser-based ultrasound applications, while losing only a factor of 7 in the detection sensitivity.   Our previous paper[9] reported values for NESD that were a factor of 2 better than those reported here but were obtained with large fringe spacings that are not compatible with applications.   The theoretical NESD curves for both positive and negative field directions are shown in Fig. 13, showing the shift in the quadrature conditions between these two field orientations.   Between the ability to tune wavelength and the ability to control the field direction, the photorefractive quantum wells have ample versatility for achieving and maintaining quadrature in practical applications.

6. DISCUSSION

The simultaneous measurements of electroabsorption and two-wave mixing presented in this paper have made it possible to determine the internal writing conversion efficiency, for the first time to our knowledge, in photorefractive quantum wells.   The value is approximately 40% at low fields and decreases with increasing field.   The internal efficiency decreases nonlinearly with field in the regime of electron velocity saturation in GaAs (which gives rise to the Gunn effect in conducting material).   The phase shift measured in the same manner agrees well with previous experimental measurements[10] and theoretical analysis.[16]   However, the linearized theory was only valid for small modulation amplitude (large β), and the theory was only stable for asymptotic velocity saturation. The linearized theory was unable to treat either large modulation amplitude (β near unity) or negative differential resistance, which is certain to be a condition in the actual experiment.   Furthermore, the theory did not predict values for the internal efficiency.   Therefore our measurements of ξ cannot currently be compared with any predicted theoretical value.   This comparison awaits

future theoretical analysis that can effectively treat the photorefractive effect in the negative differential resistance regime.

The results of laser-based ultrasound detection have demonstrated the viability of two-wave mixing in photorefractive quantum wells for performing as an adaptive beam combiner.   Our previous demonstration was performed at unworkably long fringe spacings that severely limited the field-of-view.   Furthermore, the previous results suffered from large nonadaptive intensity modulation.   The ultrasound results presented here for 30-μm fringe spacing, and without any detectable nonadaptive signal, represent an important step forward in the use of this material system for compensated interferometry applications.   All of these critical performance parameters have now been demonstrated for the quantum-well structures.   These aspects, together with the high compensation bandwidth of the quantum wells that can approach 1 MHz,[8] and with the unique ability to tune to quadrature by use of the excitonic spectral phase, make the photorefractive quantum-well devices suitable for many adaptive interferometry applications.
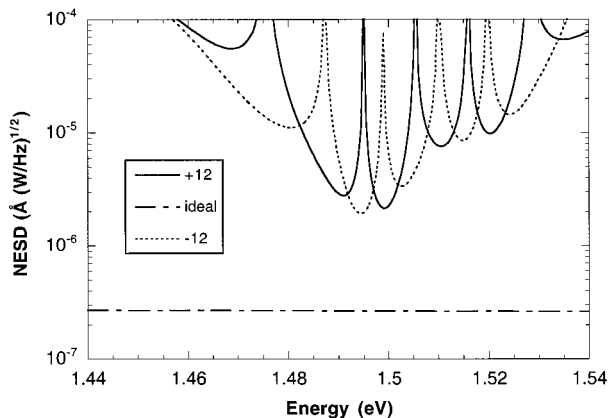
Fig. 13.   Noise-equivalent surface-displacement NESD theoretical curves from Fig. 12 to show the change in the quadrature conditions upon reversal of the electric field on the photorefractive quantum-well device.

REFERENCES

1. I. Rossomakhin and S. I. Stepanov, "Linear adaptive interferometers via diffusion recording in cubic photorefractive crystals," Opt. Commun. **86**, 199–204 (1991).
2. R. K. Ing and J.-P. Monchalin, "Broadband optical detection of ultrasound by two-wave mixing in a photorefractive crystal," Appl. Phys. Lett. **59**, 3233–3235 (1991).
3. A. Blouin and J.-P. Monchalin, "Detection of ultrasonic motion of a scattering surface by two-wave mixing in a photorefractive GaAs crystal," Appl. Phys. Lett. **65**, 932–934 (1994).
4. B. F. Pouet, R. K. Ing, S. Krishnaswamy, and D. Royer, "Heterodyne interferometer with two-wave mixing in photorefractive crystals for ultrasound detection on rough surfaces," Appl. Phys. Lett. **69**, 3782 (1996).
5. L.-A. Montmorillon, I. Biaggio, P. Delaye, J.-C. Launay, and G. Roosen, "Eye safe large field of view homodyne detection using a photorefractive CdTe:V crystal," Opt. Commun. **129**, 293 (1996).
6. P. Delaye, A. Blouin, D. Drolet, L. Montmorillon, G. Roosen, and J. Monchalin, "Detection of ultrasonic motion of a scattering surface by photorefractive InP:Fe under an applied dc field," J. Opt. Soc. Am. B **14**, 1723–1734 (1997).
7. D. D. Nolte, "Semi-insulating semiconductor heterostructures: optoelectronic properties and applications," J. Appl. Phys. **85**, 6259–6289 (1999).
8. S. Balasubramanian, I. Lahiri, Y. Ding, M. R. Melloch, and D. D. Nolte, "Two-wave mixing dynamics and nonlinear hot-electron transport in transverse-geometry photorefrac-

tive quantum wells studied by moving gratings," Appl. Phys. B **68**, 863–869 (1999).

9. I. Lahiri, L. J. Pyrak-Nolte, D. D. Nolte, M. R. Melloch, R. A. Kruger, G. D. Bacher, and M. B. Klein, "Laser-based ultrasound detection using photorefractive quantum wells," Appl. Phys. Lett. **73**, 1041–1043 (1998).

10. R. M. Brubaker, Q. N. Wang, D. D. Nolte, and M. R. Melloch, "Nonlocal photorefractive response induced by intervalley electron scattering in semiconductors," Phys. Rev. Lett. **77**, 4249–4252 (1996).

11. D. D. Nolte and M. R. Melloch, "Photorefractive quantum wells and thin films," in *Photorefractive Effects and Materials* D. D. Nolte, ed. (Kluwer Academic, Dordrecht, The Netherlands, 1995), pp. 372–451.

12. Q. N. Wang, R. M. Brubaker, D. D. Nolte, and M. R. Melloch, "Photorefractive quantum wells: transverse Franz–Keldysh geometry," J. Opt. Soc. Am. B **9**, 1626–1641 (1992).

13. I. Lahiri, "Photorefractive quantum wells: materials, devices and systems," Ph.D. dissertation (Purdue University, West Lafayette, Ind., 1998).

14. D. D. Nolte, *Book Photorefractive Effects and Materials* (Kluwer Academic, Dordrecht, The Netherlands, 1995).

15. Q. N. Wang, D. D. Nolte, and M. R. Melloch, "Two-wave mixing in photorefractive AlGaAs/GaAs quantum wells," Appl. Phys. Lett. **59**, 256–258 (1991).

16. Q. N. Wang, R. M. Brubaker, and D. D. Nolte, "Photorefractive phase shift induced by hot electron transport: multiple quantum well structures," J. Opt. Soc. Am. B **11**, 1773–1779 (1994).

17. C. V. Raman and N. S. N. Nath, "The diffraction of light by high frequency sound waves," Proc. Indian Acad. Sci. **2**, 406 (1935).

18. Y. Ding, R. M. Brubaker, D. D. Nolte, M. R. Melloch, and A. M. Weiner, "Femtosecond pulse shaping by dynamic holograms in photorefractive multiple quantum wells," Opt. Lett. **22**, 718–721 (1997).

19. Y. Ding, D. D. Nolte, M. R. Melloch, and A. M. Weiner, "Time-domain image processing using dynamic holography," IEEE J. Sel. Top. Quantum Electron. **4**, 332–341 (1998).

20. M. Dinu, K. Nakagawa, M. R. Melloch, A. M. Weiner, and D. D. Nolte, "Broadband low-dispersion diffraction of femtosecond pulses from photorefractive quantum wells," J. Opt. Soc. Am. B **17**, 1313–1319 (2000).